Systematic Computational Study of Oxide Adsorption Properties for Applications in Photocatalytic CO$_2$ Reduction

Oxana Andriuc,[†,‡] Martin Siron,[¶,‡,§,‖] and Kristin A. Persson[*,¶,⊥]

†*Department of Chemistry, University of California, Berkeley, CA 94720, USA*

‡*Liquid Sunlight Alliance and Chemical Sciences Division, Lawrence Berkeley National Laboratory, Berkeley, CA 94720, USA*

¶*Department of Materials Science and Engineering, University of California, Berkeley, CA 94720, USA*

§*Materials Science Division, Lawrence Berkeley National Laboratory, Berkeley, CA 94720, USA*

‖*Toyota Research Institute, Los Altos, CA 94022, USA*

⊥*Molecular Foundry, Lawrence Berkeley National Laboratory, Berkeley, CA 94720, USA*

E-mail: kapersson@lbl.gov

Abstract

While the adsorption properties of transition metal catalysts have been widely studied, leading to the discovery of various scaling relations, descriptors of catalytic activity, and well-established computational models, a similar understanding of semiconductor catalysts has not yet been achieved. In this work, we present a high-throughput density functional theory investigation into the adsorption properties of 5 oxides of interest to the photocatalytic CO$_2$ reduction reaction: TiO$_2$ (rutile and anatase), SrTiO$_3$,

1

NaTaO$_3$, and CeO$_2$. Using a systematic approach, we exhaustively identify unique surfaces and construct adsorption structures to undergo geometry optimizations. We then perform a data-driven analysis, which reveals the presence of weak adsorption energy scaling relations, the propensity of adsorbates of interest to interact with oxygen surface sites, and the importance of slab deformation upon adsorption. Our findings are presented in the context of experimental observations and in comparison to previously studied classes of catalysts, such as pure metals and tellurium-containing semiconductors, and reinforce the need for a comprehensive approach to the study of site-specific surface phenomena on semiconductors.

Introduction

The photocatalytic reduction of carbon dioxide is a research topic that has drawn considerable attention and effort in recent years due to its potential to address rising CO$_2$ emissions and the need for alternative fuels through a solar-driven carbon-neutral process. Despite the progress made in the field over the last several years, solar-driven CO$_2$ reduction reaction (CO$_2$RR) technologies are not yet employed at an industrial scale due to the lack of efficient, selective, and cost-effective devices that can facilitate the reaction. Much of the difficulty in designing such devices comes from the fact that they have to perform multiple roles, each posing unique sets of challenges: a good photocatalyst should be able to absorb solar light, generate charge carriers, promote their separation and transport to the corresponding reaction sites, where they can participate in the reduction and oxidation reactions.

In a previously published study, 52 materials were selected as promising photocatalysts for the CO$_2$ reduction reaction, based on a series of criteria pertaining to their synthesizability, stability in CO$_2$RR conditions, photochemical suitability, and computational cost.[1] The selection started from the 68,680 inorganic compounds existing in the Materials Project database at the time,[2] and included materials that had not yet been synthesized. The selected materials span a broad range of chemistries, including 11 oxides. In this work, we

focus on investigating the adsorption properties of the pristine surfaces of 5 of those oxides (figure 1): TiO_2 (rutile and anatase), $SrTiO_3$, $NaTaO_3$, and CeO_2. All 5 of the oxides under study have been experimentally tested for CO_2 reduction (table 1).

Although to our knowledge this is the first data-driven exploration of adsorption processes across various oxides for photocatalytic CO_2RR, various smaller-scale computational studies on the adsorption and catalytic properties of some of the materials under study have been previously published.[3–6] TiO_2 has been studied extensively as a CO_2 reduction photocatalyst, both experimentally and computationally, yet no general consensus has been reached regarding the mechanism of the reaction.[7–9] Furthermore, we note that a lot of the work on oxides without co-catalysts has focused on reduced surfaces, as oxygen vacancies have been found to play a significant role in the CO adsorption process and/or CO_2 reduction process on rutile TiO_2,[10] anatase TiO_2,[11–17] CeO_2,[18] $SrTiO_3$.[19]

The adsorbates considered in this study are CO, CHO, and H. CO was chosen as it represents one of the most common CO_2 reduction products on oxides (table 1), as well as a possible intermediate in this reaction.[7,20] CHO is another possible CO_2RR intermediate,[7,20] and studying its adsorption could also help us understand the propensity of adsorbed CO to further reduce by bonding a hydrogen atom. The set of adsorbates under study also includes H, due to its adsorption energy having been long known to be a good descriptor for the hydrogen evolution reaction (HER) activity on transition metal surfaces,[21] and HER being a competitor for CO_2RR.

| TiO₂ (anatase) | TiO₂ (rutile) | SrTiO₃ | NaTaO₃ | CeO₂ |

TiO_2 (anatase)
mp-390

TiO_2 (rutile)
mp-2657

$SrTiO_3$
mp-5229

$NaTaO_3$
mp-4170

CeO_2
mp-20194
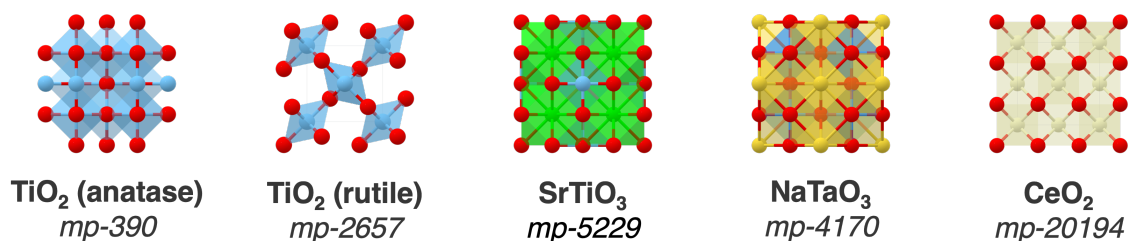
Figure 1: Oxides under study, along with their Materials Project ID. Structure graphics are from the Materials Project, generated using the Crystal Toolkit[2]

3

Table 1: Examples of CO_2 reduction products obtained on both defect-free and doped/co-catalyzed TiO_2, $SrTiO_3$, $NaTaO_3$, and CeO_2 from previously published experimental studies. Main products (if multiple) are bolded.

Material	CO_2RR products (unaided)	CO_2RR products (doped/with co-catalyst)
TiO_2 (rutile)	**CO**, CH_4 [22]	with O vacancies: **CO** (3.9× defect-free), CH_4 (5× defect-free) [22]
TiO_2 (anatase)	**CO**, CH_4 [22]	with O vacancies: **CO** (2.2× defect-free), CH_4 (13.3× defect-free) [22] supporting Pt: CH_4 [23] supporting Au: $\mathbf{CH_4}$, C_2H_6, HCHO, CH_3OH [24] doped with N & supporting Pt/Cu: $\mathbf{CH_4}$, CO, other alkanes, olefin, branched paraffin [25]
$SrTiO_3$	CO [26] *	supporting Rh: CO [27] supporting Pt: $\mathbf{CH_4}$, CO [28] nanosheets doped with Bi: **CO**, CH_4 [29]
$NaTaO_3$	**CO**, CH_3OH, CH_4 [30] **	doped with Mg/Ca/Sr/Ba/La + Ag: **CO** [31] orthorhombic + CuO: CH_3OH [32] monoclinic + Ru: $\mathbf{CH_4}$, CO [33] monoclinic + Pt: CO [33] monoclinic doped with C: HCHO [34]
CeO_2	CH_3OH [35] ***	doped with Fe/Cr : **CO**, CH_4 [36,37] homojunction + Pt: CH_4 [38] TiO_2-supported nanolayers: CO [39] O vacancies + Cu: CO [40]

* Ti-rich $SrTiO_3$ termination

** *ca.* 4.5 : 1 orthorhombic/monoclinic $NaTaO_3$

*** with O vacancies

Methods

The adsorption properties of TiO_2 (rutile and anatase), $SrTiO_3$, $NaTaO_3$, and CeO_2 were studied using our previously published automated adsorption workflow.[41] Projector-augmented wave (PAW) density functional theory calculations were performed in the Vienna Ab Initio Simulation Package (VASP 5.4.4).[42–45] The calculations were carried out using the RPBE exchange-correlation functional due to its improved performance in computing adsorption energies,[46] and Grimme's DFT-D3 correction method to account for dispersion interactions.[47] The electronic convergence criterion was set to 1×10^{-5} eV and the ionic convergence criterion was force-based (0.05 eV/Å). The energy cut-off for the plane-wave basis set was set to 400 eV. For slab and adsorption structure geometry optimizations the k-points mesh was defined as $30/a \times 30/b \times 30/c$. For bulk geometry optimizations and slab and adsorption structure static calculations, the default pymatgen k-point settings were used.[41,48] A sample set of input files is provided in the Supplementary Information.

Slab structures were generated for terminations up to a Miller index of 1, with a minimum vacuum of 12 Å, a minimum height of 7 Å, and a minimum length and width of 10 Å. The chosen lateral dimensions of the slabs ensure that the computed adsorption properties are for the low coverage case, allowing us to focus on surface-adsorbate interactions in the absence of adsorbate-adsorbate contributions. Dipole corrections to the potential and forces perpendicular to the surface were added to slab calculations.[49] In this work, slabs are identified by their Miller index as well as the fractional shift in the c direction where the termination lies. For some Miller indices we therefore report multiple slabs, as they correspond to different unique planes that are parallel along that direction. Negative c-shift values correspond to slabs that are built by inversion from their positive c-shift slab counterparts with nonequivalent top and bottom terminations.

Adsorption structures were generated based on the Delaunay triangulation method and adsorbate-surface distance optimization step as described in previous work.[41,50] CO and CHO were both positioned with C towards the surface, CO perpendicular to the surface and

https://doi.org/10.26434/chemrxiv-2024-051v5 **ORCID:** https://orcid.org/0000-0002-4011-3339 Content not peer-reviewed by ChemRxiv. **License:** CC BY-NC-ND 4.0

CHO with H and O pointing away from the surface (figure 2). The CHO study was limited to TiO$_2$ surfaces only.
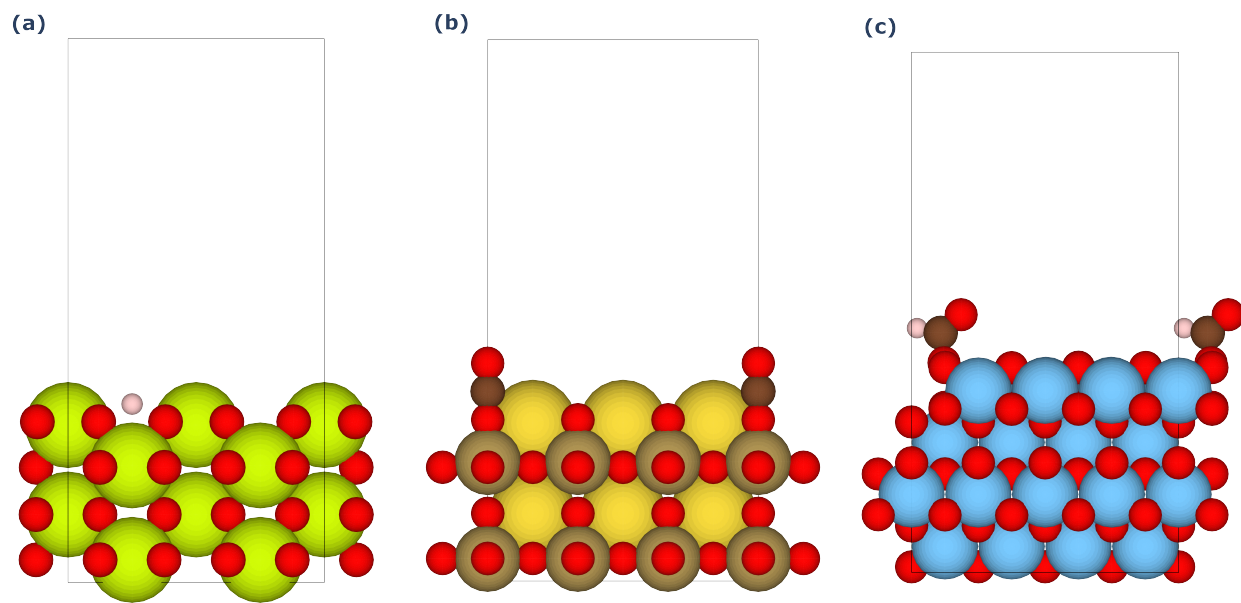
Figure 2: Examples of input adsorption structures: (a) H on a CeO$_2$ (110) surface, (b) CO on a NaTaO$_3$ (100) surface, (c) CHO on a rutile TiO$_2$ (100) surface

Adsorption properties, including the adsorption energy, were computed as described in previous work.[41] Reference energies for the adsorbates were calculated as described in previous work[51] from the energies of H$_2$, CO, and H$_2$O as obtained from DFT geometry optimizations of $10 \times 10 \times 10$ Å cells containing each of the molecules. The reference energies for H and CHO were therefore computed as:

$$E_H = \frac{1}{2}E_{\text{H}_2} \tag{1}$$

$$E_{CHO} = E_{CO} + \frac{1}{2}E_{\text{H}_2} \tag{2}$$

In addition to the calculations done through the adsorption workflow, the Local Orbital Basis Suite Toward Electronic-Structure Reconstruction (LOBSTER)[52–56] implementation in Atomate[57] was used to perform bonding analysis. Moreover, slab deformation energies were computed as the difference between the energy of the slab structure in the geometry it

relaxes to upon adsorption and the energy of the empty relaxed slab structure.

Results and discussion

All five oxides under study have been previously synthesized, and the bulk lattice parameters computed in this work are in good agreement with experimentally measured literature values (table 2). Overall, 22 surfaces across the 5 materials were considered, with their cleavage energies listed in table 2. We note that the listed cleavage energies were computed from geometry optimizations in which the bottom surface of the slab was fixed. Moreover, some of the slabs are not symmetric (i.e. do not have equivalent top and bottom terminations). Therefore, our computed cleavage energies cannot be directly compared with experimental surface energies, but can nevertheless serve as a computational indicator of instability and therefore likelihood of adsorption structure geometry optimizations to converge successfully.

The 300+ adsorption structures with successfully converged geometry optimizations were first filtered to remove any geometries in which bonds within the adsorbate (if any) were broken, as well as cases in which the surface reconstructed significantly (slab atoms separated from the surface, or multiple bonds within the slab broken/formed). The lowest (most negative) adsorption energy for each of the surfaces was selected as representative for that surface and used when investigating the existence of adsorption energy scaling relations.

Our computed adsorption energies generally align well with literature values. The CO adsorption energy we calculate on rutile TiO_2 (110) of -9.8 kcal/mol is in good agreement with the -9.9 kcal/mol CO binding energy for this surface as determined through thermal desorption experiments.[62] Similarly to previous computational studies,[63,64] we identify more favorable adsorption on CeO_2 (110) than on CeO_2 (111) for both CO and H. The most favorable CO adsorption energy computed for the $SrTiO_3$ (100) surface (-0.51 eV) is in good agreement with previously calculated values (-0.45 eV)[19,65] Discrepancies between our values and those reported in previously published computational studies[3–6,16,66] can mainly

7

Table 2: Bulk lattice parameters (both from this work and from experimental studies reported in literature) and surface cleavage energies computed in this work for the oxides under study

Material [MP ID]	Lattice parameters from this work (Å,°)	Lattice parameters from literature (Å,°)	Surface [c shift]: cleavage energy (J/m^2)
TiO$_2$ (rutile) [mp-2657]	$a = 4.60$ $b = 4.60$ $c = 2.96$ $\alpha, \beta, \gamma = 90$	$a = 4.58$ $b = 4.58$ $c = 2.95$ $\alpha, \beta, \gamma = 90$[58]	(001) [0.250]: 2.06 (100) [0.250]: 1.34 (101) [0.500]: 1.55 (110) [0.500]: 1.36 (111) [-0.446]: 6.70 (111) [0.446]: 2.55
TiO$_2$ (anatase) [mp-390]	$a = 3.79$ $b = 3.79$ $c = 9.47$ $\alpha, \beta, \gamma = 90$	$a = 3.73$ $b = 3.73$ $c = 9.37$ $\alpha, \beta, \gamma = 90$[58]	(001) [0.125]: 1.19 (100) [0.250]: 1.19 (101) [-0.020]: 4.48 (101) [-0.355]: 3.40 (101) [0.125]: 1.66 (101) [0.355]: 3.64 (101) [0.625]: 1.01 (110) [0.250]: 1.76 (111) [0.020]: 2.40 (111) [0.125]: 3.04
SrTiO$_3$ [mp-5229]	$a = 3.92$ $b = 3.92$ $c = 3.92$ $\alpha, \beta, \gamma = 90$	$a = 3.91$ $b = 3.91$ $c = 3.91$ $\alpha, \beta, \gamma = 90$[59]	(100) [-0.250]: 1.31 (100) [0.250]: 1.27
NaTaO$_3$ [mp-4170]	$a = 3.96$ $b = 3.96$ $c = 3.96$ $\alpha, \beta, \gamma = 90$	$a = 3.93$ $b = 3.93$ $c = 3.93$ $\alpha, \beta, \gamma = 90$[60]	(100) [-0.250]: 1.37 (100) [0.250]: 1.25
CeO$_2$ [mp-20194]	$a = 5.42$ $b = 5.42$ $c = 5.42$ $\alpha, \beta, \gamma = 90$	$a = 5.41$ $b = 5.41$ $c = 5.41$ $\alpha, \beta, \gamma = 90$[61]	(110) [0.250]: 1.23 (111) [0.500]: 0.79

8

be attributed to differences in the adsorbate coverage and the level of theory used.
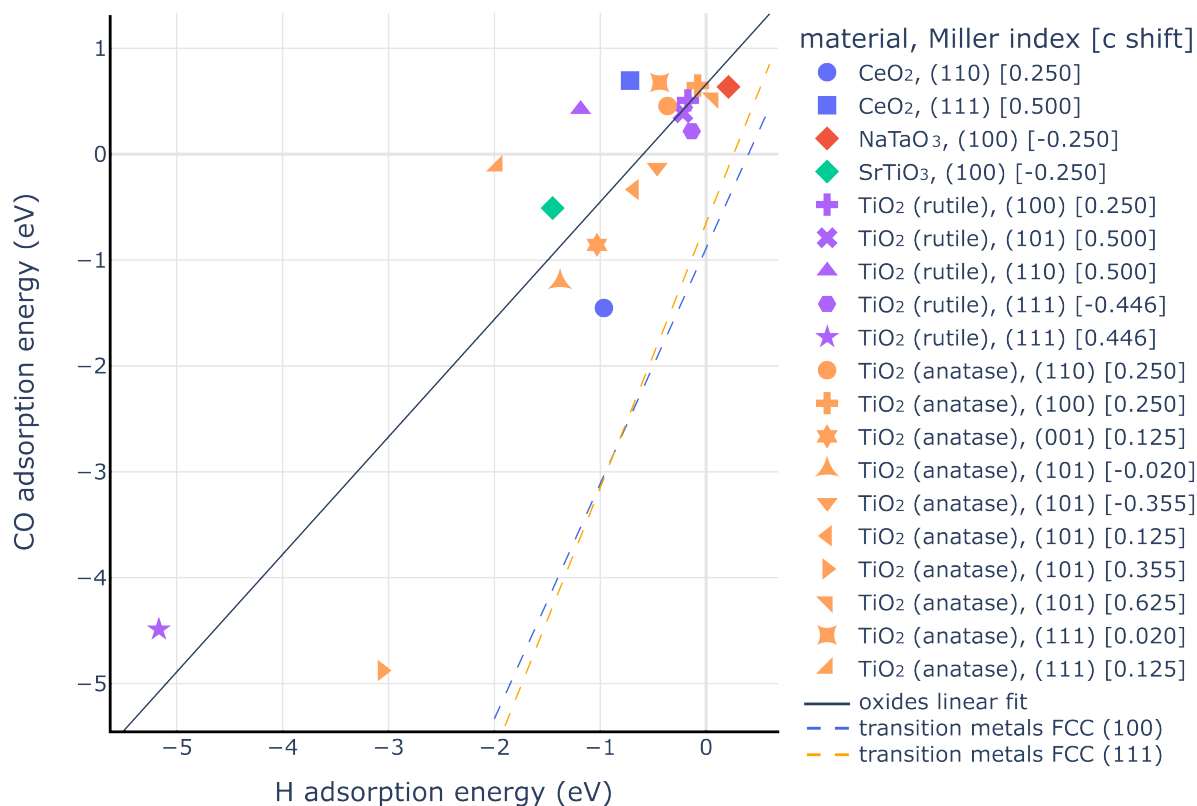
Figure 3: CO adsorption energies as a function of H adsorption energies for each oxide surface under study. For each surface, the most stable adsorption site is plotted (which might not be the same between CO and H). The linear fit for the oxides data is shown in black (slope: 1.11, intercept: 0.66, R^2: 0.77, p-value: 8.36×10^{-7}, standard error: 0.15). Linear scaling relations for the (100) and (111) surfaces of FCC transition metals from literature are shown in dashed lines.[67]

Visualizing the CO adsorption energies as a function of the H adsorption energies for the oxide surfaces reveals a weak linear relationship (figure 3). This plot also shows how roughly half of the surfaces under consideration do not exhibit any favorable CO adsorption (positive CO adsorption energies). Conversely, for all surfaces but two the most stable H adsorption structure exhibits a negative adsorption energy. We also identify two surfaces ((111) TiO_2 rutile and (101) TiO_2 anatase) with strongly negative adsorption energies for both CO and H. When compared to the scaling relations observed on face-centered cubic transition metal

9

surfaces,[67] oxides exhibit more favorable H adsorption energies for a given CO adsorption energy. Furthermore, we note that none of the surfaces under study have a negative CO adsorption energy but a positive H adsorption energy. These observations are generally in accordance with the known issues of CO_2RR selectivity over HER.[30,68]
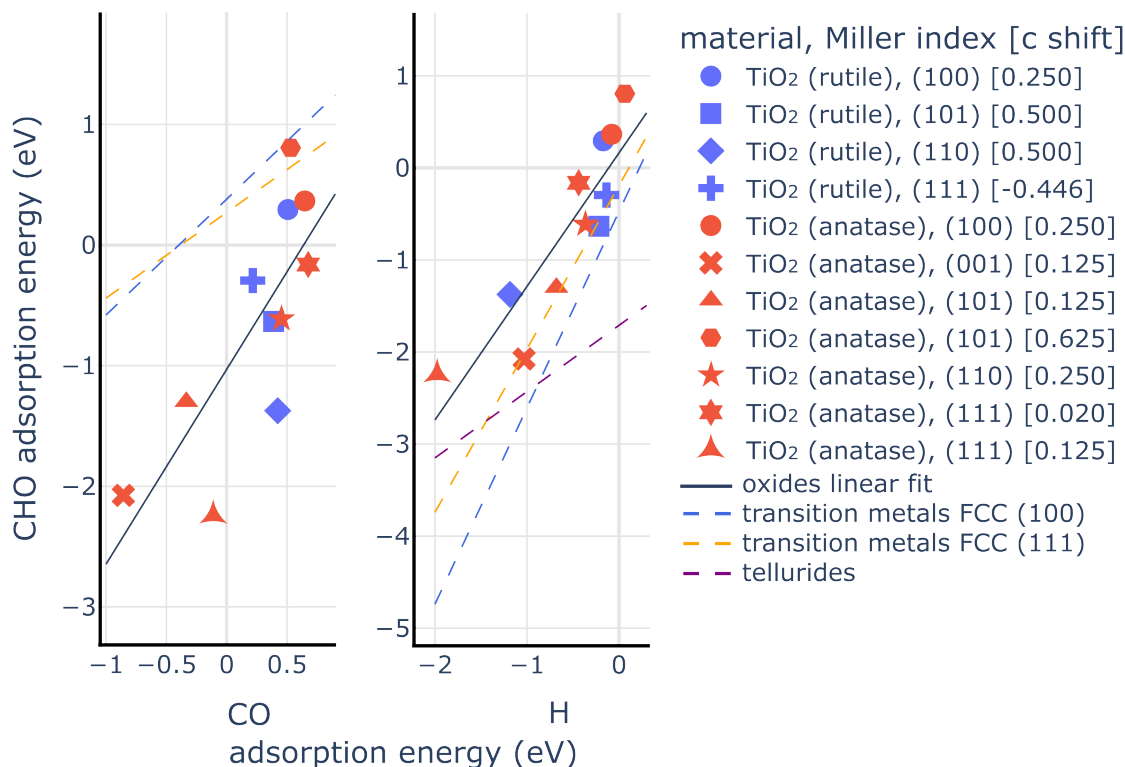
Figure 4: CHO adsorption energies as a function of CO and H adsorption energies for the TiO_2 surfaces under study. For each surface, the most stable adsorption site is plotted (which might not be the same between CHO, CO, and H). The linear fit for the oxides data is shown in black (CHO vs. CO slope: 1.62, intercept: -1.03, R^2: 0.59, p-value: 0.0053, standard error: 0.44; CHO vs. H slope: 1.45, intercept: 0.16, R^2: 0.80, p-value: 2.23×10^{-4}, standard error: 0.25). Linear scaling relations for the (100) and (111) surfaces of FCC transition metals[67] and for tellurides[69] are shown in dashed lines.

Our computed data also reveals linear correlations between CHO adsorption energies and CO/H adsorption energies for TiO_2 surfaces (figure 4). It must be noted though that compared to transition metal scaling relations,[67] which are found for specific sites on a given termination across various materials, in this work we are comparing the most stable

10

sites on different terminations. Nevertheless, when compared to the transition metal scaling relations for both (100) and (111) surfaces, TiO_2 surfaces generally exhibit more favorable CHO adsorption energies for a given CO adsorption energy. This could indicate that, barring other factors, TiO_2 could lead to more reduced products, beyond CO. It could also offer support for the presence of a CHO-intermediate in the CO_2RR mechanism on TiO_2, such as the glyoxal pathway.[7] Nevertheless, without further kinetic studies, which are beyond the scope of this work, these hypotheses remain speculation. When compared to tellurium-containing semiconductors,[69] TiO_2 shows much more favorable H adsorption energies for a given CHO adsorption energy. This could indicate an increased suppression of HER for the newly emergent class of telluride CO_2RR photocatalysts, given the known CO_2RR vs. HER selectivity issue for TiO_2.[68]
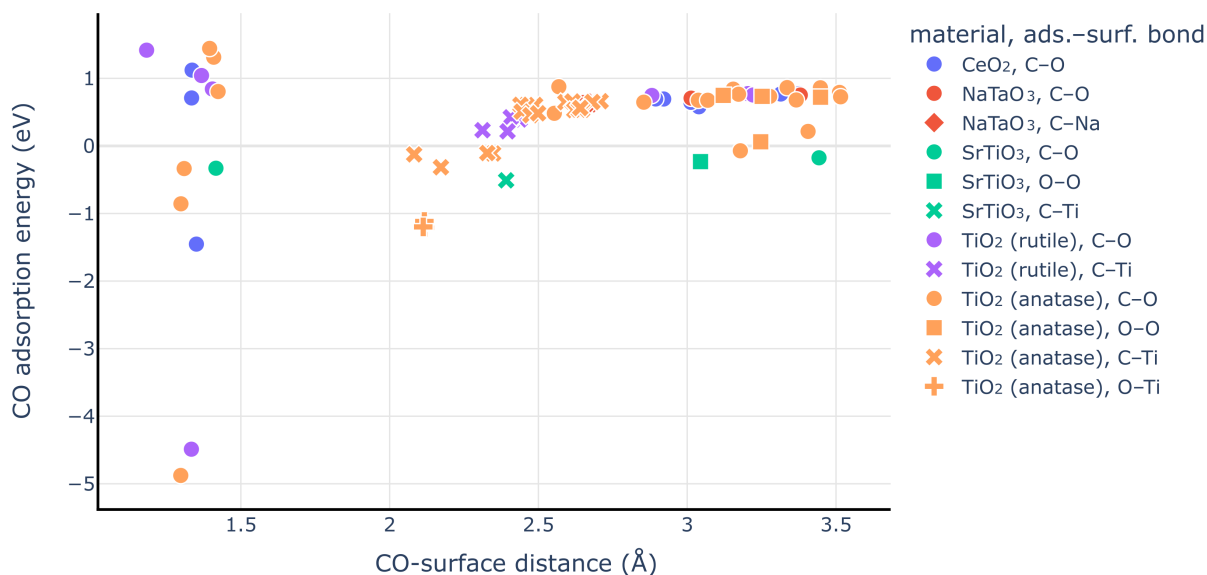
Figure 5: CO adsorption energy as a function of CO-surface distance across all adsorption sites over all the oxide surfaces under study. The CO-surface distance is defined as the smallest distance between C or O within the CO adsorbate and any surface atom. The data points are colored by material and their symbols represent the adsorbate element and surface element involved in this smallest-distance CO-surface interaction.

In order to establish guidelines for CO_2RR photocatalyst design, we investigated element-

specific propensity towards adsorption. Across all CO adsorption structures under study, we find that only adsorbate C-surface O structures have CO-surface distances that can qualify as chemical bonding ($< 1.5\,\text{Å}$), and they span quite a broad range of adsorption energies, down to $-5\,\text{eV}$ (figure 5). All other structures exhibit physisorption, with the CO adsorbate relaxing at distances of over $2\,\text{Å}$ from the surface. The preference for CO adsorption through C on rutile and anatase TiO_2 is consistent with previously published results.[4–6,16,66] We also note that with the exception of two $NaTaO_3$ adsorption structures, where CO is closest to a Na site, and one $SrTiO_3$ structure, where CO is closest to a Ti site, the nearest site to CO is always an O site in non-TiO_2 oxides. In the case of both rutile and anatase TiO_2 we observe interactions with both Ti and O. This is in contrast with the previously studied tellurium-containing semiconductors, for which CO binds to a variety of cationic sites.[69] Previous work using *Ab Initio* Molecular Dynamics identified both Ti and O sites on the rutile TiO_2 (110) surface as favorable for CO_2 adsorption,[70] which in light of our results could suggest that a reduction from CO_2 to CO could occur on various sites on the rutile surface. Our data also reveals that in the case of some $SrTiO_3$ and anatase TiO_2 structures, the CO adsorbate rotates to the point of approaching the surface through O rather than C and interacting most closely with O or Ti surface sites. This observation prompts the need for future work expanding the study to CO adsorption structures in which the CO adsorbate is positioned at different angles with respect to the surface in the input structures, including oriented vertically with the oxygen end towards the slab.

In the case of H adsorption affinity (figure 6), we note once again that the shortest H-surface distances, corresponding to chemisorption, occur exclusively in cases in which H is closest to a surface O site. This is expected given the relative electronegativity of the elements involved. Nevertheless, unlike CO, H interacts with all elements present across the oxides under study, even if it is through weaker physisorption, at distances of over $1.7\,\text{Å}$. These weak H interactions at non-CO adsorption sites could indicate that these hydrogens could preferentially participate in the CO_2 reduction reaction rather than in HER: the positive

12
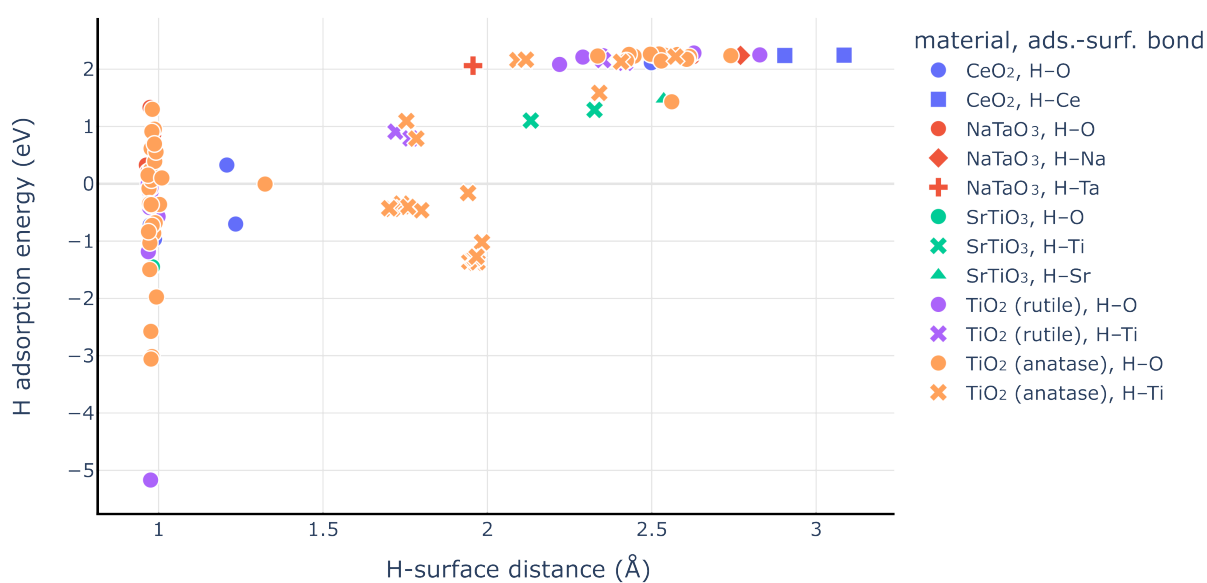
Figure 6: H adsorption energy as a function of H-surface distance across all adsorption sites over all the oxide surfaces under study. The H-surface distance is defined as the smallest distance between the H adsorbate and any surface atom. The data points are colored by material and their symbols represent the surface element involved in this smallest-distance H-surface interaction.

adsorption energy of H at these sites is not likely to lead to increased HER activity, but its favorable position could make it available for more reduced CO_2RR products, as observed in table 1. Overall, both in the case of CO and H adsorption, the variety of adsorption modalities supports the need for a systematic approach in the study of adsorption on oxide surfaces.
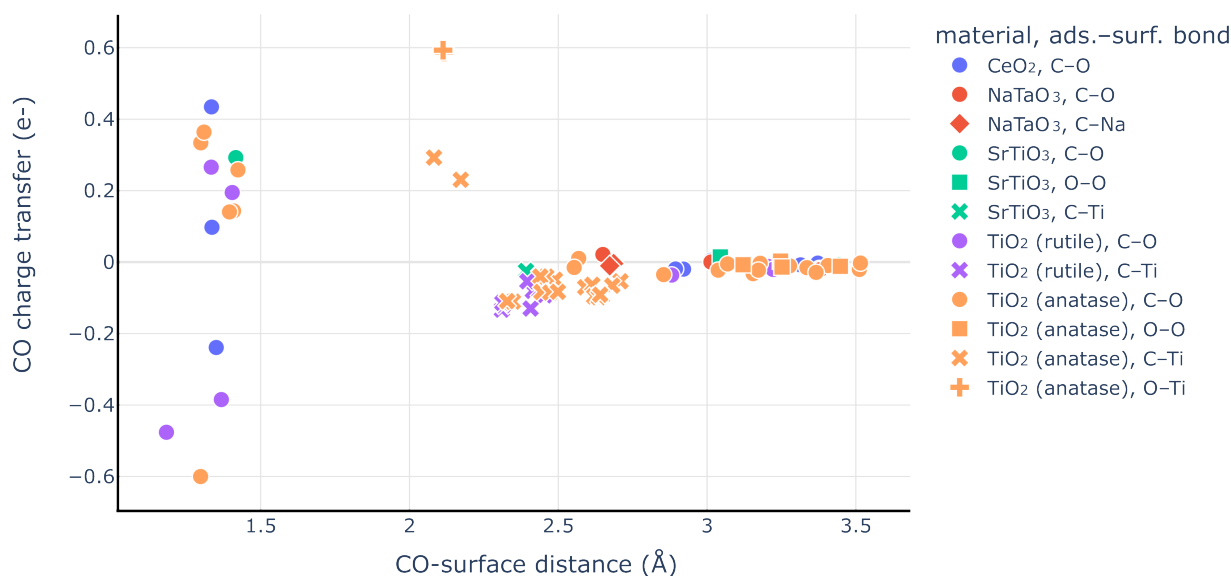
Figure 7: CO charge transfer as a function of CO-surface distance across all adsorption sites over all the oxide surfaces under study. The CO charge transfer is computed using the DDEC6 charge partitioning analysis[71–74] and it is positive if charge is transferred from the surface to the adsorbate and negative if it is transferred from the adsorbate to the surface. The CO-surface distance is defined as the smallest distance between C or O within the CO adsorbate and any surface atom. The data points are colored by material and their symbols represent the adsorbate element and surface element involved in this smallest-distance CO-surface interaction.

Most surfaces under study show a negligible charge transfer to CO, with weak, often unfavorable physisorption (figures 5, 7), which is consistent with CO being the main CO_2RR product (table 1). However, we do identify some TiO_2, CeO_2, and $SrTiO_3$ surfaces that show a transfer of charge from the surface to CO upon adsorption, in addition to stronger CO-surface bonding. This is consistent with some of the more reduced products observed

14

on some of these surfaces and highlights their potential as CO_2RR photocatalysts.
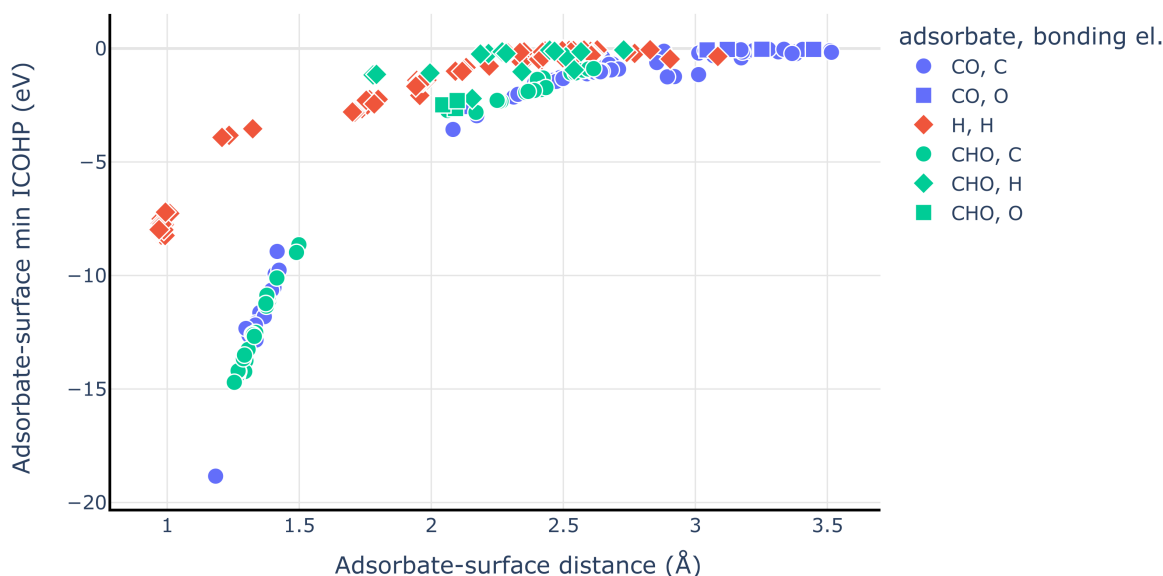
Figure 8: The minimum ICOHP value between any adsorbate atom and a surface atom as a function of the shortest distance between any adsorbate atom and a surface atom across all adsorption structures under study. The data points are colored by adsorbate and their symbols represent the adsorbate atom that is closest to the surface.

In order to gain more insight into the bonding between the adsorbates and the oxide surfaces, we performed a crystal orbital Hamilton population (COHP) analysis[53–56] on the adsorption structures. We focused on one descriptor of bonding strength, the integrated crystal orbital Hamilton population (ICOHP). As more negative ICOHP values correspond to stronger covalent interactions,[75] we chose the lowest (most negative) ICOHP value between any adsorbate atom and any surface atom as representative for the strongest adsorbate-surface bond, and also computed summed ICOHP values across all adsorbate atoms for each adsorption structure.

Firstly, we investigated the relationship between the minimum ICOHP as described above against the adsorbate-surface distance, defined as the shortest distance between an adsorbate atom and a surface atom (figure 8). As expected, we observed a positive correlation between the two, with bonding strength plateauing in the physisorption regime, at distances over

15

2 Å. At short distances, the H adsorption structures appear as outliers to the CO and CHO trend. This can be explained by the strong short-range covalent bonds that H forms with other nonmetals;[76,77] as previously discussed, in all of these structures, H is closest to O (figure 6). These results, including the H-bonded outliers, are consistent with previous findings.[75]

In an attempt to further understand the bonding in the oxide adsorption structures, we employed a distortion/interaction model.[78,79] The adsorption energy can be split into the following contributions:

$$\Delta E_{ads} = \Delta E_{dist}^{slab} + \Delta E_{dist}^{ads} + \Delta E_{int} \tag{3}$$

where ΔE_{dist}^{slab} is the slab distortion energy as the slab relaxes upon adsorption, ΔE_{dist}^{ads} is the adsorbate distortion energy as the adsorbate relaxes upon adsorption, and ΔE_{int} is the interaction energy between the slab and the adsorbate. We note that in our calculations for H and CHO, since our adsorbate reference energies are computed according to equation 1, ΔE_{dist}^{ads} also comprises the difference between our reference energies and the energy of the free adsorbate. This represents just a constant shift in all of our computed values and will therefore not influence our conclusions.

For monoatomic adsorbates, such as H, equation 3 is simply:

$$\Delta E_{ads} = \Delta E_{dist}^{slab} + \Delta E_{int} \tag{4}$$

By subtracting the slab distortion energy from the adsorption energy, we therefore can assess the contributions from the adsorbate deformation and the bonding interaction to the adsorption energy. As the adsorption structures under study have been filtered to remove cases in which adsorbate geometries changed significantly upon adsorption, we assume that even in the case of CO and CHO, most of the difference between the adsorption energy and the slab distortion energy comes from the adsorbate-surface interaction.

In the case of H adsorption, where $\Delta E_{ads}^{H} - \Delta E_{dist}^{slab}$ is simply the H-surface interaction

16
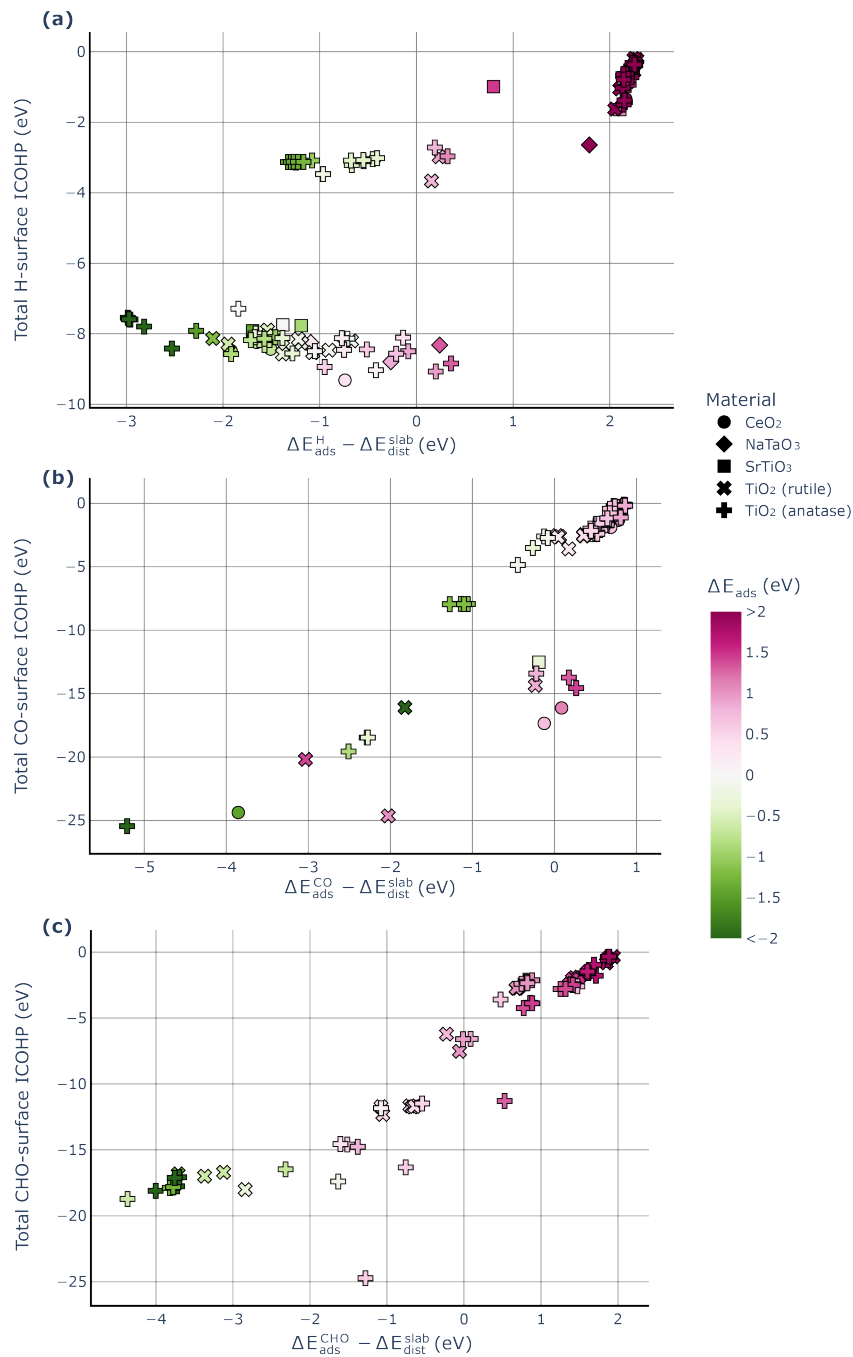
Figure 9: The total ICOHP value between all adsorbate atoms and all surface atoms as a function of the difference between the adsorption energy and the slab deformation energy for (a) H adsorption structures, (b) CO adsorption structures, and (c) CHO adsorption structures. The data points are colored by adsorption energies and their symbols represent the material.
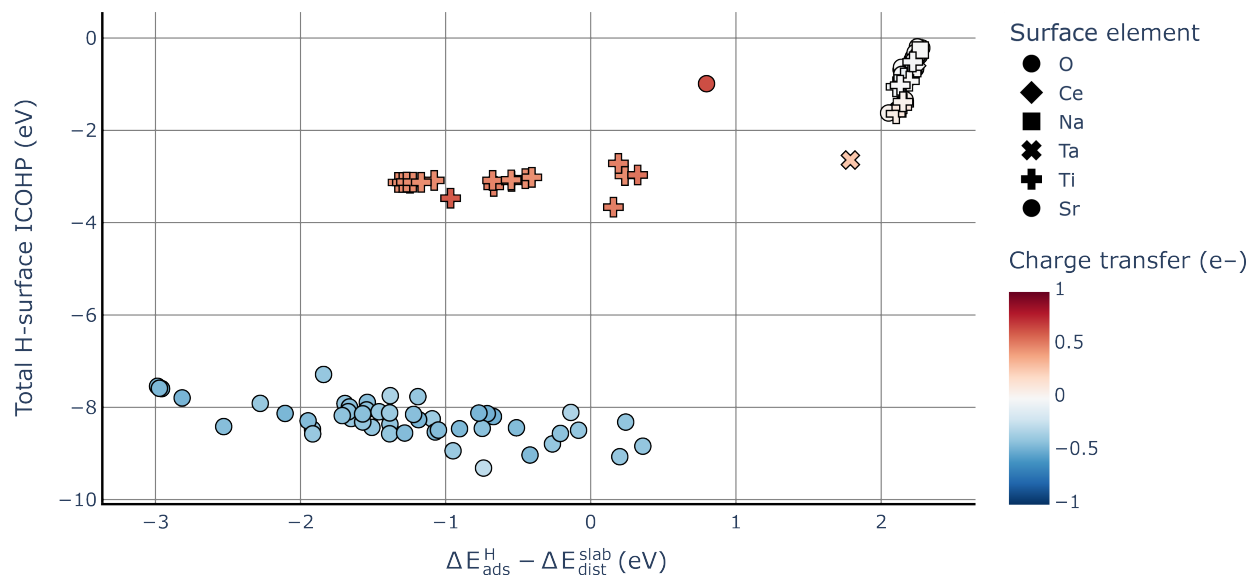
Figure 10: The total ICOHP value between H and all surface atoms as a function of the difference between the adsorption energy and the slab deformation energy. The data points are colored by charge transfer values and their symbols represent the surface atom that H is closest to. Positive charge transfer values indicate charge transferred from the surface to the adsorbate and negative values indicate charge transferred from the adsorbate to the surface.

energy (ΔE_{int}), we notice that generally, across all materials, ΔE_{int} follows the same trend as the adsorption energy, with low adsorption energies towards the negative x axis end and more positive adsorption energies towards the positive x end (figure 9(a)). This indicates that surface relaxation upon H adsorption does not significantly affect adsorption. However, there is no strong correlation between the total ICOHP value and the adsorption or interaction energy. To understand why that is the case, we can visualize the same data, this time color-coded by charge transfer and with symbols representing the nearest surface element to H (figure 10). This plot reveals that the structures for which the total ICOHP does not correlate positively with the interaction energy are those for which there is a non-negligible charge transfer between the slab and the adsorbate. This is consistent with the ICOHP being a measure of covalent interactions and therefore reveals that in most H adsorption structures under consideration the degree of ionic bonding dictates the overall strength of H-surface interaction. We can identify 3 distinctive regions: 1. the subset of structures in which H is

18

closest to O atoms and donates charge to the surface; in this region, the covalent interaction strength is relatively constant, while the ionic contributions dictate the overall value of the interaction energy (in the broad range of $-3\,\text{eV}$ to $0.5\,\text{eV}$), 2. the subset of structures in which H is closest to Ti sites and receives charge from the surface; in this region, the covalent interaction strength is relatively constant, but weaker than in the case of structures with H-O bonding, while the ionic contributions dictate the overall value of the interaction energy (in the range of $-1.5\,\text{eV}$ to $0.5\,\text{eV}$), and 3. a region of weak covalent bonding, negligible charge-transfer, high positive interaction energy, and high adsorption energy which comprises of H bonded to various elements. As we can dismiss the last region as structures with unfavorable H interactions, we can conclude that in cases where H does interact favorably with the slab, it is the ionic contributions to these interactions that determine their strength.

Unlike in the case of the H adsorption structures, a positive correlation between $\Delta E_{ads}^{CO} - \Delta E_{dist}^{slab}$ and ΔE_{ads}^{CO} is not as obvious, especially at more negative ICOHP values (figure 9(b)). We can therefore conclude that the interplay between surface deformation and adsorbate deformation becomes significant for CO adsorption. This highlights the importance of looking beyond the local environment when studying or designing CO_2RR photocatalysts. Once again in contrast with H adsorption structures, there is a generally positive correlation between the CO-structure ICOHP and $\Delta E_{ads}^{CO} - \Delta E_{dist}^{slab}$. This indicates that most CO-surface interactions are covalent in nature.

Finally, for CHO adsorption structures we observe a positive correlation between ICOHP, $\Delta E_{ads}^{CHO} - \Delta E_{dist}^{slab}$, and the CHO adsorption energy (figure 9(c)). This suggests that most CHO-surface interactions have a covalent character and that the slab deformation energy does not significantly affect the adsorption energy. In light of the CO observations as discussed in the previous paragraph, these results indicate that the geometry changes upon CO adsorption, which are not necessary for CHO adsorption, could be one of the factors contributing to CO_2RR not proceeding past CO formation on the oxides under study.

19

Conclusions

In order to further understand the propensity of a series of oxides previously selected as possible photocatalysts for CO_2RR towards actually carrying CO_2 reduction, we performed a data-driven high-throughput study of the adsorption properties of these oxides. Through this work, we identified a series of weak scaling relations between CO, H, and CHO adsorption energies, established element-based design rules (most favorable CO and H adsorption interactions always occur in the proximity of O sites), and identified slab deformation as a significant factor in CO adsorption and ionic contributions as the determining factors in the value of H-surface interaction energy.

Furthermore, we present this work as a strong case for the importance of the previously published semiconductor adsorption workflow.[41] In the case of complex, often unstable surfaces, such as those of semiconductors, the study of their adsorption properties cannot (yet) be limited to one adsorption site for a given surface across all materials, as often is the case for the more well-behaved, well-understood metallic systems.

We also use this work as another argument towards the importance of further investigating the tellurides presented in previous work[69] as more promising CO_2RR catalysts. The tellurium-containing semiconductors exhibit more deviation from scaling relations and, as discussed at times in this paper, their adsorption properties position them as an exciting class of materials to explore.

Finally, while many of the conclusions drawn throughout this paper are, for now, speculations, we expect this work to become crucial if and when a better mechanistic understanding for CO_2RR on oxides, or semiconductors more broadly, is built. Having a better understanding of the mechanism of this reaction, along with microkinetic modeling, will allow for a more direct connection between the breadth of adsorption properties computed here and measures of CO_2RR efficiency.

Acknowledgement

References

(1) Singh, A. K.; Montoya, J. H.; Gregoire, J. M.; Persson, K. A. Robust and synthesizable photocatalysts for CO_2 reduction: a data-driven materials discovery. *Nature Communications* **2019**, *10*, 443.

(2) Jain, A.; Ong, S. P.; Hautier, G.; Chen, W.; Richards, W. D.; Dacek, S.; Cholia, S.; Gunter, D.; Skinner, D.; Ceder, G.; Persson, K. A. Commentary: The Materials Project: A materials genome approach to accelerating materials innovation. *APL Materials* **2013**, *1*, 011002.

(3) Islam, M. M.; Calatayud, M.; Pacchioni, G. Hydrogen Adsorption and Diffusion on the Anatase TiO_2(101) Surface: A First-Principles Investigation. *The Journal of Physical Chemistry C* **2011**, *115*, 6809–6814, Publisher: American Chemical Society.

(4) Yang, Z.; Wu, R.; Zhang, Q.; Goodman, D. W. First-principles study of the adsorp-

tion of CO on TiO_2(110). *Physical Review B* **2001**, *63*, 045419, Publisher: American Physical Society.

(5) Scaranto, J.; Giorgianni, S. A quantum-mechanical study of CO adsorbed on TiO_2: A comparison of the Lewis acidity of the rutile (110) and the anatase (101) surfaces. *Journal of Molecular Structure: THEOCHEM* **2008**, *858*, 72–76.

(6) Setvin, M. et al. A Multitechnique Study of CO Adsorption on the TiO_2 Anatase (101) Surface. *The Journal of Physical Chemistry C* **2015**, *119*, 21044–21052.

(7) Habisreutinger, S. N.; Schmidt-Mende, L.; Stolarczyk, J. K. Photocatalytic Reduction of CO_2 on TiO_2 and Other Semiconductors. *Angewandte Chemie International Edition* **2013**, *52*, 7372–7408.

(8) Liu, L.; Li, Y. Understanding the Reaction Mechanism of Photocatalytic Reduction of CO2 with H2O on TiO2-Based Photocatalysts: A Review. *Aerosol and Air Quality Research* **2014**, *14*, 453–469.

(9) Ip, C. M.; Troisi, A. A computational study of the competing reaction mechanisms of the photo-catalytic reduction of CO_2 on anatase(101). *Physical Chemistry Chemical Physics* **2016**, *18*, 25010–25021.

(10) Zhao, Y.; Wang, Z.; Cui, X.; Huang, T.; Wang, B.; Luo, Y.; Yang, J.; Hou, J. What Are the Adsorption Sites for CO on the Reduced TiO_2 (110)-1 × 1 Surface? *Journal of the American Chemical Society* **2009**, *131*, 7958–7959.

(11) Ji, Y.; Luo, Y. Theoretical Study on the Mechanism of Photoreduction of CO_2 to CH_4 on the Anatase TiO_2 (101) Surface. *ACS Catalysis* **2016**, *6*, 2018–2025.

(12) Ji, Y.; Luo, Y. New Mechanism for Photocatalytic Reduction of CO_2 on the Anatase TiO_2 (101) Surface: The Essential Role of Oxygen Vacancy. *Journal of the American Chemical Society* **2016**, *138*, 15896–15902.

(13) Liu, J.-Y.; Gong, X.-Q.; Alexandrova, A. N. Mechanism of CO_2 Photocatalytic Reduction to Methane and Methanol on Defected Anatase TiO_2 (101): A Density Functional Theory Study. *The Journal of Physical Chemistry C* **2019**, *123*, 3505–3511.

(14) Liu, J.-Y.; Gong, X.-Q.; Li, R.; Shi, H.; Cronin, S. B.; Alexandrova, A. N. (Photo)Electrocatalytic CO_2 Reduction at the Defective Anatase TiO_2 (101) Surface. *ACS Catalysis* **2020**, *10*, 4048–4058.

(15) Sorescu, D. C.; Al-Saidi, W. A.; Jordan, K. D. CO_2 adsorption on $TiO_2(101)$ anatase: A dispersion-corrected density functional theory study. *The Journal of Chemical Physics* **2011**, *135*, 124701.

(16) Lustemberg, P. G.; Scherlis, D. A. Monoxide carbon frequency shift as a tool for the characterization of TiO_2 surfaces: Insights from first principles spectroscopy. *The Journal of Chemical Physics* **2013**, *138*, 124702.

(17) He, H.; Zapol, P.; Curtiss, L. A. A Theoretical Study of CO_2 Anions on Anatase (101) Surface. *The Journal of Physical Chemistry C* **2010**, *114*, 21474–21481, Publisher: American Chemical Society.

(18) Kumari, N.; Haider, M. A.; Agarwal, M.; Sinha, N.; Basu, S. Role of Reduced CeO2(110) Surface for CO2 Reduction to CO and Methanol. *The Journal of Physical Chemistry C* **2016**, *120*, 16626–16635, Publisher: American Chemical Society.

(19) Jiang-Ni, Y.; Zhi-Yong, Z.; Jun-Feng, Y.; Fu-Chun, Z. First Principles Study of Adsorption and Reaction of CO on $SrTiO_3$ (100) Surface: the Role of Surface Oxygen Vacancies. *Chinese Physics Letters* **2010**, *27*, 017101.

(20) Kumari, N.; Sinha, N.; Haider, M. A.; Basu, S. CO_2 Reduction to Methanol on CeO_2 (110) Surface: a Density Functional Theory Study. *Electrochimica Acta* **2015**, *177*, 21–29.

(21) Conway, B. E.; Bockris, J. O. Electrolytic Hydrogen Evolution Kinetics and Its Relation to the Electronic and Adsorptive Properties of the Metal. *The Journal of Chemical Physics* **1957**, *26*, 532–541.

(22) Liu, L.; Zhao, H.; Andino, J. M.; Li, Y. Photocatalytic CO_2 Reduction with H_2O on TiO_2 Nanocrystals: Comparison of Anatase, Rutile, and Brookite Polymorphs and Exploration of Surface Chemistry. *ACS Catalysis* **2012**, *2*, 1817–1828, Publisher: American Chemical Society.

(23) Uner, D.; Oymak, M. M. On the mechanism of photocatalytic CO_2 reduction with water in the gas phase. *Catalysis Today* **2012**, *181*, 82–88.

(24) Hou, W.; Hung, W. H.; Pavaskar, P.; Goeppert, A.; Aykol, M.; Cronin, S. B. Photocatalytic Conversion of CO_2 to Hydrocarbon Fuels via Plasmon-Enhanced Absorption and Metallic Interband Transitions. *ACS Catalysis* **2011**, *1*, 929–936, Publisher: American Chemical Society.

(25) Varghese, O. K.; Paulose, M.; LaTempa, T. J.; Grimes, C. A. High-Rate Solar Photocatalytic Conversion of CO_2 and Water Vapor to Hydrocarbon Fuels. *Nano Letters* **2009**, *9*, 731–737, Publisher: American Chemical Society.

(26) Luo, C.; Zhao, J.; Li, Y.; Zhao, W.; Zeng, Y.; Wang, C. Photocatalytic CO_2 reduction over $SrTiO_3$: Correlation between surface structure and activity. *Applied Surface Science* **2018**, *447*, 627–635.

(27) Yan, B.; Wu, Q.; Cen, J.; Timoshenko, J.; Frenkel, A. I.; Su, D.; Chen, X.; Parise, J. B.; Stach, E.; Orlov, A.; Chen, J. G. Highly active subnanometer Rh clusters derived from Rh-doped $SrTiO_3$ for CO_2 reduction. *Applied Catalysis B: Environmental* **2018**, *237*, 1003–1011.

(28) Wu, X.; Wang, C.; Wei, Y.; Xiong, J.; Zhao, Y.; Zhao, Z.; Liu, J.; Li, J. Multifunctional photocatalysts of Pt-decorated 3DOM perovskite-type $SrTiO_3$ with enhanced CO_2 ad-

sorption and photoelectron enrichment for selective CO_2 reduction with H_2O to CH_4. *Journal of Catalysis* **2019**, *377*, 309–321.

(29) Pan, L.; Mei, H.; Zhu, G.; Li, S.; Xie, X.; Gong, S.; Liu, H.; Jin, Z.; Gao, J.; Cheng, L.; Zhang, L. Bi selectively doped $SrTiO_3$-x nanosheets enhance photocatalytic CO_2 reduction under visible light. *Journal of Colloid and Interface Science* **2022**, *611*, 137–148.

(30) Fresno, F.; Jana, P.; Reñones, P.; Coronado, J. M.; Serrano, D. P.; De La Peña O'Shea, V. A. CO_2 reduction over $NaNbO_3$ and $NaTaO_3$ perovskite photocatalysts. *Photochemical & Photobiological Sciences* **2017**, *16*, 17–23.

(31) Nakanishi, H.; Iizuka, K.; Takayama, T.; Iwase, A.; Kudo, A. Highly Active $NaTaO_3$-Based Photocatalysts for CO_2 Reduction to Form CO Using Water as the Electron Donor. *ChemSusChem* **2017**, *10*, 112–118.

(32) Xiang, T.; Xin, F.; Chen, J.; Wang, Y.; Yin, X.; Shao, X. Selective photocatalytic reduction of CO_2 to methanol in CuO-loaded $NaTaO_3$ nanocubes in isopropanol. *Beilstein Journal of Nanotechnology* **2016**, *7*, 776–783.

(33) Li, M.; Li, P.; Chang, K.; Wang, T.; Liu, L.; Kang, Q.; Ouyang, S.; Ye, J. Highly efficient and stable photocatalytic reduction of CO_2 to CH_4 over Ru loaded $NaTaO_3$. *Chemical Communications* **2015**, *51*, 7645–7648.

(34) Mora-Hernandez, J. M.; Huerta-Flores, A. M.; Torres-Martínez, L. M. Photoelectrocatalytic characterization of carbon-doped $NaTaO_3$ applied in the photoreduction of CO_2 towards the formaldehyde production. *Journal of CO2 Utilization* **2018**, *27*, 179–187.

(35) Hezam, A.; Namratha, K.; Drmosh, Q. A.; Ponnamma, D.; Wang, J.; Prasad, S.; Ahamed, M.; Cheng, C.; Byrappa, K. CeO_2 Nanostructures Enriched with Oxygen Vacancies for Photocatalytic CO_2 Reduction. *ACS Applied Nano Materials* **2020**, *3*, 138–148, Publisher: American Chemical Society.

(36) Wang, Y.; Wang, F.; Chen, Y.; Zhang, D.; Li, B.; Kang, S.; Li, X.; Cui, L. Enhanced photocatalytic performance of ordered mesoporous Fe-doped CeO_2 catalysts for the reduction of CO_2 with H_2O under simulated solar irradiation. *Applied Catalysis B: Environmental* **2014**, *147*, 602–609.

(37) Wang, Y.; Bai, X.; Wang, F.; Kang, S.; Yin, C.; Li, X. Nanocasting synthesis of chromium doped mesoporous CeO_2 with enhanced visible-light photocatalytic CO_2 reduction performance. *Journal of Hazardous Materials* **2019**, *372*, 69–76.

(38) Li, P.; Zhou, Y.; Zhao, Z.; Xu, Q.; Wang, X.; Xiao, M.; Zou, Z. Hexahedron Prism-Anchored Octahedronal CeO2: Crystal Facet-Based Homojunction Promoting Efficient Solar Fuel Synthesis. *Journal of the American Chemical Society* **2015**, *137*, 9547–9550, Publisher: American Chemical Society.

(39) Jiao, J.; Wei, Y.; Zhao, Z.; Liu, J.; Li, J.; Duan, A.; Jiang, G. Photocatalysts of 3D Ordered Macroporous TiO_2-Supported CeO_2 Nanolayers: Design, Preparation, and Their Catalytic Performances for the Reduction of CO_2 with H_2O under Simulated Solar Irradiation. *Industrial & Engineering Chemistry Research* **2014**, *53*, 17345–17354, Publisher: American Chemical Society.

(40) Wang, M.; Shen, M.; Jin, X.; Tian, J.; Li, M.; Zhou, Y.; Zhang, L.; Li, Y.; Shi, J. Oxygen Vacancy Generation and Stabilization in CeO_2–x by Cu Introduction with Improved CO_2 Photocatalytic Reduction Activity. *ACS Catalysis* **2019**, *9*, 4573–4581, Publisher: American Chemical Society.

(41) Andriuc, O.; Siron, M.; Montoya, J. H.; Horton, M.; Persson, K. A. Automated Adsorption Workflow for Semiconductor Surfaces and the Application to Zinc Telluride. *Journal of Chemical Information and Modeling* **2021**, *61*, 3908–3916.

(42) Kresse, G.; Furthmüller, J. Efficiency of ab-initio total energy calculations for metals

and semiconductors using a plane-wave basis set. *Computational Materials Science* **1996**, *6*, 15–50.

(43) Kresse, G.; Furthmüller, J. Efficient iterative schemes for *ab initio* total-energy calculations using a plane-wave basis set. *Physical Review B* **1996**, *54*, 11169–11186.

(44) Blöchl, P. E. Projector augmented-wave method. *Physical Review B* **1994**, *50*, 17953–17979.

(45) Kresse, G.; Joubert, D. From ultrasoft pseudopotentials to the projector augmented-wave method. *Physical Review B* **1999**, *59*, 1758–1775.

(46) Hammer, B.; Hansen, L. B.; Nørskov, J. K. Improved adsorption energetics within density-functional theory using revised Perdew-Burke-Ernzerhof functionals. *Physical Review B* **1999**, *59*, 7413–7421.

(47) Grimme, S.; Antony, J.; Ehrlich, S.; Krieg, H. A consistent and accurate *ab initio* parametrization of density functional dispersion correction (DFT-D) for the 94 elements H-Pu. *The Journal of Chemical Physics* **2010**, *132*, 154104.

(48) Ong, S. P.; Richards, W. D.; Jain, A.; Hautier, G.; Kocher, M.; Cholia, S.; Gunter, D.; Chevrier, V. L.; Persson, K. A.; Ceder, G. Python Materials Genomics (pymatgen): A robust, open-source python library for materials analysis. *Computational Materials Science* **2013**, *68*, 314–319.

(49) Neugebauer, J.; Scheffler, M. Adsorbate-substrate and adsorbate-adsorbate interactions of Na and K adlayers on Al(111). *Physical Review B* **1992**, *46*, 16067–16080.

(50) Montoya, J. H.; Persson, K. A. A high-throughput framework for determining adsorption energies on solid surfaces. *npj Computational Materials* **2017**, *3*, 14.

(51) Torrisi, S. B.; Singh, A. K.; Montoya, J. H.; Biswas, T.; Persson, K. A. Two-dimensional

27

forms of robust CO_2 reduction photocatalysts. *npj 2D Materials and Applications* **2020**, *4*, 24.

(52) Nelson, R.; Ertural, C.; George, J.; Deringer, V. L.; Hautier, G.; Dronskowski, R. LOB-STER: Local orbital projections, atomic charges, and chemical-bonding analysis from projector-augmented-wave-based density-functional theory. *Journal of Computational Chemistry* **2020**, *41*, 1931–1940.

(53) Dronskowski, R.; Bloechl, P. E. Crystal orbital Hamilton populations (COHP): energy-resolved visualization of chemical bonding in solids based on density-functional calculations. *The Journal of Physical Chemistry* **1993**, *97*, 8617–8624.

(54) Deringer, V. L.; Tchougréeff, A. L.; Dronskowski, R. Crystal Orbital Hamilton Population (COHP) Analysis As Projected from Plane-Wave Basis Sets. *The Journal of Physical Chemistry A* **2011**, *115*, 5461–5466, Publisher: American Chemical Society.

(55) Maintz, S.; Deringer, V. L.; Tchougréeff, A. L.; Dronskowski, R. Analytic projection from plane-wave and PAW wavefunctions and application to chemical-bonding analysis in solids. *Journal of Computational Chemistry* **2013**, *34*, 2557–2567, _eprint: https://onlinelibrary.wiley.com/doi/pdf/10.1002/jcc.23424.

(56) Maintz, S.; Deringer, V. L.; Tchougréeff, A. L.; Dronskowski, R. LOB-STER: A tool to extract chemical bonding from plane-wave based DFT. *Journal of Computational Chemistry* **2016**, *37*, 1030–1035, _eprint: https://onlinelibrary.wiley.com/doi/pdf/10.1002/jcc.24300.

(57) Mathew, K. et al. Atomate: A high-level interface to generate, execute, and analyze computational materials science workflows. *Computational Materials Science* **2017**, *139*, 140–152.

(58) Diebold, U. The surface science of titanium dioxide. *Surface Science Reports* **2003**, *48*, 53–229.

(59) Bednorz, J.; Scheel, H. Flame-fusion growth of $SrTiO_3$. *Journal of Crystal Growth* **1977**, *41*, 5–12.

(60) Kennedy, B. J.; Prodjosantoso, A. K.; Howard, C. J. Powder neutron diffraction study of the high temperature phase transitions in $NaTaO_3$. *Journal of Physics: Condensed Matter* **1999**, *11*, 6319–6327.

(61) Prieur, D.; Bonani, W.; Popa, K.; Walter, O.; Kriegsman, K. W.; Engelhard, M. H.; Guo, X.; Eloirdi, R.; Gouder, T.; Beck, A.; Vitova, T.; Scheinost, A. C.; Kvashnina, K.; Martin, P. Size Dependence of Lattice Parameter and Electronic Structure in CeO_2 Nanoparticles. *Inorganic Chemistry* **2020**, *59*, 5760–5767.

(62) Linsebigler, A.; Lu, G.; Yates, J. T. CO chemisorption on TiO_2 (110): Oxygen vacancy site influence on CO adsorption. *The Journal of Chemical Physics* **1995**, *103*, 9438–9443.

(63) Yang, Z.; Woo, T. K.; Hermansson, K. Strong and weak adsorption of CO on CeO_2 surfaces from first principles calculations. *Chemical Physics Letters* **2004**, *396*, 384–392.

(64) Vicario, G.; Balducci, G.; Fabris, S.; de Gironcoli, S.; Baroni, S. Interaction of Hydrogen with Cerium Oxide Surfaces: a Quantum Mechanical Computational Study. *The Journal of Physical Chemistry B* **2006**, *110*, 19380–19385, Publisher: American Chemical Society.

(65) Jiang-Ni, Y.; Zhi-Yong, Z.; Fu-Chun, Z. Adsorption and Reaction of CO on (100) Surface of $SrTiO_3$ by Density Function Theory Calculation. *Chinese Physics Letters* **2008**, *25*, 3364.

(66) Sorescu, D. C.; Yates, J. T. Adsorption of CO on the TiO_2 (110) Surface: A Theoretical Study. *The Journal of Physical Chemistry B* **1998**, *102*, 4556–4565.

(67) Shi, C.; Hansen, H. A.; Lausche, A. C.; Nørskov, J. K. Trends in electrochemical CO_2 reduction activity for open and close-packed metal surfaces. *Physical Chemistry Chemical Physics* **2014**, *16*, 4720–4727, Publisher: The Royal Society of Chemistry.

(68) Nguyen, T. P.; Nguyen, D. L. T.; Nguyen, V.-H.; Le, T.-H.; Vo, D.-V. N.; Trinh, Q. T.; Bae, S.-R.; Chae, S. Y.; Kim, S. Y.; Le, Q. V. Recent Advances in TiO_2-Based Photocatalysts for Reduction of CO_2 to Fuels. *Nanomaterials* **2020**, *10*, 337.

(69) Siron, M.; Andriuc, O.; Persson, K. A. Data-Driven Investigation of Tellurium-Containing Semiconductors for CO2 Reduction: Trends in Adsorption and Scaling Relations. *The Journal of Physical Chemistry C* **2022**, *126*, 13224–13236, Publisher: American Chemical Society.

(70) Klyukin, K.; Alexandrov, V. CO_2 Adsorption and Reactivity on Rutile TiO_2 (110) in Water: An *Ab Initio* Molecular Dynamics Study. *The Journal of Physical Chemistry C* **2017**, *121*, 10476–10483.

(71) Manz, T. A.; Limas, N. G. Introducing DDEC6 atomic population analysis: part 1. Charge partitioning theory and methodology. *RSC Advances* **2016**, *6*, 47771–47801.

(72) Limas, N. G.; Manz, T. A. Introducing DDEC6 atomic population analysis: part 2. Computed results for a wide range of periodic and nonperiodic materials. *RSC Advances* **2016**, *6*, 45727–45747.

(73) Manz, T. A. Introducing DDEC6 atomic population analysis: part 3. Comprehensive method to compute bond orders. *RSC Adv.* **2017**, *7*, 45552–45581.

(74) Limas, N. G.; Manz, T. A. Introducing DDEC6 atomic population analysis: part 4. Efficient parallel computation of net atomic charges, atomic spin moments, bond orders, and more. *RSC Advances* **2018**, *8*, 2678–2707.

(75) Naik, A. A.; Ertural, C.; Dhamrait, N.; Benner, P.; George, J. A Quantum-Chemical Bonding Database for Solid-State Materials. *Scientific Data* **2023**, *10*, 610, Number: 1 Publisher: Nature Publishing Group.

(76) Benson, S. W. III - Bond energies. *Journal of Chemical Education* **1965**, *42*, 502, Publisher: American Chemical Society.

(77) Gordy, W. A Relation between Bond Force Constants, Bond Orders, Bond Lengths, and the Electronegativities of the Bonded Atoms. *The Journal of Chemical Physics* **1946**, *14*, 305–320.

(78) Ess, D. H.; Houk, K. N. Distortion/Interaction Energy Control of 1,3-Dipolar Cycloaddition Reactivity. *Journal of the American Chemical Society* **2007**, *129*, 10646–10647, Publisher: American Chemical Society.

(79) Hong, X.; Chan, K.; Tsai, C.; Nørskov, J. K. How Doped MoS_2 Breaks Transition-Metal Scaling Relations for CO_2 Electrochemical Reduction. *ACS Catalysis* **2016**, *6*, 4428–4437.

TOC Graphic